Identifying a Critical Micelle Temperature in Simulations of Disordered Asymmetric Diblock Copolymer Melts

Anshul Chawla, Frank S. Bates, Kevin D. Dorfman,* and David C. Morse[†]

Department of Chemical Engineering and Materials Science,

University of Minnesota, 421 Washington Ave. SE, Minneapolis, MN 55455, USA

(Dated: August 27, 2021)

Experiments on asymmetric diblock copolymers at temperatures slightly above the order-disorder transition (ODT) indicate the existence of a dense fluid of micelles. Molecular dynamics simulations are used here to identify a higher critical micelle temperature below which micelles appear. The onset of micellization occurs very near where self-consistent field theory predicts an ODT.

In melts of highly asymmetric diblock copolymers at temperatures slightly above the order disorder temperature (ODT), the disordered phase contains a dense liquid of spherical micelles [1–7]. At the ODT, these micelles crystallize. Simple analogies to the theory of binary surfactant-solvent mixtures, which exhibit a critical micelle concentration [8], suggest that a micelle forming one-component system should exhibit a critical micelle temperature (CMT) at which micelles appear with decreasing temperature over a rather narrow range of temperatures [9, 10]. The ODT is clearly identifiable in scattering experiments by the appearance of Bragg peaks. Clear experimental identification of a CMT has, however, remained elusive.

In this work, we study the appearance of micelles in large-scale simulations of a coarse-grained simulation model of AB diblock copolymers with well characterized thermodynamic properties and an experimentally relevant chain length. Simulations allow access to information about molecular clusters that is not easily accessible in experiments. We confirm that spherical micelles do indeed appear and proliferate over a narrow range of temperatures, and show that this occurs very near where self-consistent field theory (SCFT) predicts the simultaneous emergence and crystallization of micelles.

Micelle formation in compositionally asymmetric block copolymers above bears similarities to the formation of a disordered bicontinuous morphology above the ODT in symmetric block copolymers. Both are manifestations of strong correlations in the disordered phase, which critically influence order-disorder transitions in finite molecular weight systems [11–15], although many aspects of both structure and dynamics are qualitatively different. Whereas the bicontinuous state has recently been described theoretically [16–18] and imaged using electron microscopy [19–22], micelle formation, and the existence of a CMT, remains largely unexplored notwithstanding publication of several provocative TEM images two decades ago [5, 6]. The importance of this ubiquitous state of condensed matter has become increasingly evident with the discovery of dodecagonal quasicrystals and numerous Frank-Kasper phases in a host of soft materials [13, 23–30]. Recent reports of metastable particle-based

phases that evolve from the quenched disordered liquid [31–33] underscore the significance of this unique, and poorly understood state, motivating the work described here.

Experimental evidence for the existence of micelles in the disordered phase comes primarily from microscopy and scattering experiments. The most direct evidence is from transmission electron micrographs showing disordered arrangments of spherical micelles [5, 6]. Results of small angle X-ray (SAXS) and neutron (SANS) scattering from the disordered phase near the ODT exhibit a secondary shoulder in plots of scattered intensity I(q) vs. wavenumber q, at a wavenumber well above the primary peak wavenumber q^* . This secondary feature is believed to be a consequence of liquid-like correlations in micelle positions, and has been successfully modelled using liquid-state theories for hard spheres [1–4, 7].

Quantitative understanding of self-assembly in sphere forming systems relies heavily on predictions of self-consistent field theory (SCFT) [13, 31, 34–38]. Consider a melt of AB diblock copolymers with a volume fraction f < 0.2 for the minority B block, an overall degree of polymerization N, Flory-Huggins parameter χ , monomer concentration c and statistical segment length b for both A and B monomers. SCFT predicts that micelles should both appear and crystallize at a transition value of χN , denoted here by $(\chi N)_{\rm odt}^{\rm scf}$. SCFT is believed to be exact in the limit of infinite invariant degree of polymerization $\overline{N} = N(cb^3)^2$ [11, 16, 17, 39], but ignores the existence of strong correlations in the disordered phase in systems with experimentally relevant molecular weights.

Wang et al. [10] have used SCFT to compute the free energy of formation for an isolated spherical micelle within a disordered phase, denoted by W_m . SCFT yields a prediction of the form $W_m = k_B T \overline{N}^{1/2} \tilde{W}_m(\chi N, f)$, where \tilde{W}_m is a dimensionless function of χN and f. The value of χN above which $W_m < 0$ at a given f, denoted here by $(\chi N)_{\rm m}^{\rm scf}$, is found to be very near but slightly greater than $(\chi N)_{\rm odt}^{\rm scf}$. For example, for f = 0.1, $(\chi N)_{\rm odt}^{\rm scf} = 47.95$ and $(\chi N)_{\rm m}^{\rm scf} = 48.14$ [10]. This small difference is a result of a weak attraction between micelles in a crystal, but is negligible for purposes of the analysis given here. SCFT predicts the existence of strongly

segregated micelle cores even at $(\chi N)_{\rm odt}^{\rm scf}$, with a minority volume fraction near 90 % at the center of the micelle for $f \simeq 0.1$. Upon allowing for micelle translational entropy, Wang et al. predict a micelle volume fraction proportional to e^{-W_m/k_BT} and a rapid increase in micelle concentration over a narrow range of values of χN of width $\overline{N}^{-1/2}$ near $(\chi N)_{\rm m}^{\rm scf}$. These conclusions are consistent with those of an earlier analysis by Dormidontova and Lodge [9] that relied on a less accurate strong segregation model for W_m , but that allowed for effects of micelle interactions that Wang et al. neglected. While these theoretical predictions are enticing, neither experiments nor simulations have thus far allowed a definitive identification of a CMT in compositionally asymmetric diblock copolymers.

Recent progress in the interpretation of coarse-grained molecular simulations has enabled increasingly precise comparisons of simulations to SCFT, and thereby sharpened our understanding of the strengths and weaknesses of SCFT. The comparison to SCFT predictions given here was enabled by this prior work. Glaser, Medapuram, Morse and coworkers introduced a method of calibrating the dependence of the effective χ parameter on simulation input parameters that has allowed consistent results to be obtained from a variety of different coarse-grained models [16, 17, 40–43]. Their analysis showed that strong correlations appear within the disordered phase when χN exceeds $(\chi N)_{\text{odt}}^{\text{scf}}$, while the actual ODT occurs at an elevated value $(\chi N)_{\rm odt}$ that exhibits a universal dependence on \overline{N} . Notably, SCFT was found to yield rather accurate predictions for properties of ordered lamellar and hexagonal phases [16, 17, 43]. These results thus provided evidence for the accuracy of SCFT predictions for self-assembled structures such as lamellae or micelles, while also emphasizing the failure of a random-mixing description of the disordered phase near the ODT. The assumption that SCFT accurately predicts the free energy required to form an isolated micelle also suggests a hypothesis that micelles should first appear at a value of χN very near $(\chi N)_{\rm odt}^{\rm scf}$.

In this work, we study the appearance of micelles in molecular dynamics (MD) simulations of an AB diblock copolymer melt. Simulations are performed in constant pressure, constant temperature ensemble. Quantitative comparison to theoretical predictions is enabled by using a simulation model for which the relationship between χ and simulation parameters has been established previously [16, 17]. The model used here is referred to as model S2 in Refs. 16, 17 or model D3 in Ref. 42, for which $\overline{N}/N = (cb^3)^2 = 59.7$. In all work reported here, each chain has N = 64 beads, with 8 B beads and 56 A beads, giving f = 1/8 and $\overline{N} = 3820$. SCFT predicts $(\chi N)_{\text{odt}}^{\text{scf}} = 36.6$ for f = 1/8. A harmonic bond potential acts between adjacent beads within each chain. A non-bonded pair potential of the form $V(r) = \frac{1}{2}\epsilon_{ij}(1 - r/\sigma)^2$

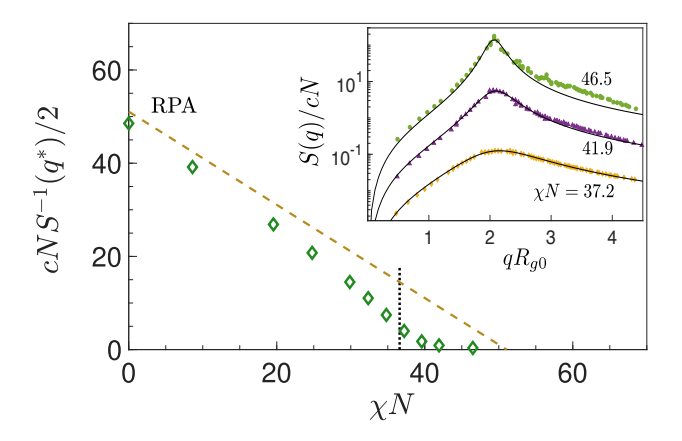


FIG. 1. Main plot: Non-dimensional inverse peak intensity $cNS^{-1}(q^*)/2$ vs. χN . The dashed line shows the RPA prediction. The dotted vertical line indicates $(\chi N)_{\rm odt}^{\rm sef}=36.6$. Inset: Structure factor S(q) vs. qR_{g0} at three nearby values of χN , where $R_{g0}=b\sqrt{N/6}$. Solid lines show a fit to the RPA functional form.

acts between beads of types i and j that are separated by a distance r less than a cutoff σ , with V(r)=0 for $r>\sigma$. The parameter $\alpha=(\epsilon_{AB}-\epsilon_{AA})/k_BT$ is varied to modify the effective χ parameter, while the pressure, temperature, bond spring constant and $\epsilon_{AA}=\epsilon_{BB}$ are held at constant values chosen in previous work. Simulations were performed on systems of approximately 5×10^5 beads. Further simulation details are given in Supplemental Material [44].

Fig. 1 shows the behavior of the structure factor S(q), akin to the scattering intensity measured in SAXS and SANS experiments. We define $S(q) = V^{-1} \langle |\psi(\mathbf{q})|^2 \rangle$, where $\psi(\mathbf{q}) = \int d\mathbf{r} \ \psi(\mathbf{r}) e^{i\mathbf{q}\cdot\mathbf{r}}, \ \psi(\mathbf{r}) = [c_A(\mathbf{r}) - c_B(\mathbf{r})]/2$, $c_i(\mathbf{r})$ is the concentration of i monomers, V is system volume, and $q = |\mathbf{q}|$. All values of χN reported in this paper were calculated using a calibration of χ obtained in previous work [16, 17] (see Table S1).

The inset of Fig. 1 shows S(q) vs. q at three values of χN near $(\chi N)_{\rm odt}^{\rm scf}=36.6.$ Solid lines show fits of S(q) to a functional form $S(q) = KS_{RPA}(q)$, in which $S_{RPA}(q)$ is the random-phase approximation (RPA) prediction, and in which R_q , χ and the prefactor K have all been treated as adjustable parameters. Comparison to this fit helps emphasize the existence at $\chi N = 46.5$ and 41.9 of a weak shoulder in S(q) at $qR_{g0} \simeq 3.4$, which we identify here by the failure of an attempted fit to the RPA. This feature is absent for all $\chi N < (\chi N)_{\rm odt}^{\rm scf}$, for which S(q) is fit well by the RPA functional form. An analogous feature has been observed in scattering scattering experiments performed at temperatures slightly above the ODT [1–3, 6, 7], which appears at wavenumbers with approximately the same relationship to the peak wavenumber as that found here, though the magnitude of this secondary feature varies in experiments depending on proximity to the ODT and \overline{N} .

The main plot in Fig. 1 shows the behavior of the

normalized inverse of the peak intensity $cNS^{-1}(q^*)/2$ vs. χN . The dashed line shows the RPA prediction for this quantity, computed without adjustable parameters. The actual dependence of $S^{-1}(q^*)$ on χN shows a falling point of inflection near $(\chi N)_{\text{odt}}^{\text{scf}}$ that separates a region of slight negative curvature at lower χN from a region of positive curvature at higher χN . Notably, this behavior is different from that found in symmetric and modestly asymmetric copolymers, for which this plot instead exhibits a uniformly positive curvature, reflecting the tendency of $S(q^*)$ to increase more slowly with increasing χN than predicted by the RPA. The behavior seen here instead indicates a tendency for the $S(q^*)$ to increase more rapidly than predicted by the RPA for χN near $(\chi N)_{\text{odt}}^{\text{scf}}$. An alternative view of these data is shown in Fig. S1 by plotting $S(q^*)/S_{RPA}(q^*)$ vs. χN , which shows a rapid increase near $(\chi N)_{\text{odt}}^{\text{scf}}$. We show below that this increased scattering coincides with the appearance of micelles.

In an MD simulation, potential micelles may be identified by finding clusters of molecules with minority B block beads in close contact. We identify such clusters using a criterion in which two molecules are taken to belong to the same cluster if the distance between any two B beads on these different molecules is less than 0.8σ . Let n denote the number of molecules in such a cluster.

Fig. 2 shows the fraction x_n of chains within clusters of aggregation number n plotted vs. n at several values of χN . At $\chi N = 0$, geometrical clusters exist only as a result of random intermolecular minority block contacts. In this limit, x_n decreases monotonically with increasing n but still includes a non-negligible value for clusters with tens of molecules. The distribution evolves slowly with increasing χN up to the next displayed value of $\chi N = 34.8$, which is slightly less than $(\chi N)_{\rm odt}^{\rm scf} = 36.6$. At this value, x_n remains monotonically decreasing but shows enhanced frequency for larger n as a result of increasingly strong composition fluctuations. For $\chi N >$ 37.2, however, the distribution develops a local maximum at a most-probable aggregation number $n^* \simeq 80 - 140$ that grows larger and more distinct with increasing χN , signalling the appearance of proper micelles. We will show in a future paper that the secondary maximum at $n \simeq 2n^* \simeq 280$ at $\chi N = 46.5$ is due to clusters containing two micelles with cores joined by a narrow throat.

Fig. 3 describes the spatial structure of clusters with aggregation numbers within a range chosen to correspond to potential micelles. At values of χN for which the plot of x_n vs. n from Fig. 2 shows a local maximum, properties in Fig. 3 are computed by considering clusters with n ranging from the least probable value (the minimum in Fig. 2) to 1.6 times the most probable value. A range of n=30-160 is instead used at lower values of χN for which no local maximum exists.

Fig. 3a shows the average $\overline{\phi}_B(r)$ of the effective volume fraction $\phi_B(r)$ of B (minority) beads that belong to

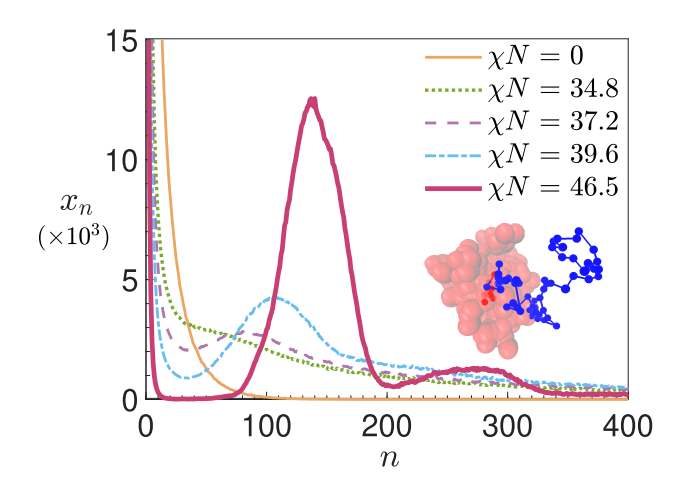


FIG. 2. Average mole fraction x_n of chains within clusters of aggregation number n, vs. n. The inset shows a cluster snapshot, with B (core) beads in translucent red, with one chain highlighted with blue A beads and red B beads.

a cluster as a function of distance r from the center of mass (COM) of all B beads in the cluster. We define the value of ϕ_B within a small region of volume ΔV to be equal to a ratio $\phi_B = m_B/c\Delta V$, where m_B is the number of B beads in that region that belong to molecules in a cluster, where $c \simeq 1.5\sigma^{-3}$ is the macroscopic bead number concentration and $c\Delta V$ is the average total number of beads in a region of volume ΔV . The quantity $\overline{\phi}_B(r)$ is an average of ϕ_B for a thin spherical annulus centered around the COM, averaged over time and over clusters with n in the chosen range.

Consider the increase of $\overline{\phi}_B(r=0)$ at the cluster COM with increasing χN shown in Fig. 3a. Note that the displayed values of χN are not evenly spaced. At $\chi N=0$, the value of $\overline{\phi}_B(r=0)\simeq 0.19$ is only slightly greater than spatial average value of f=0.125, indicating the diffuse nature of these purely geometrical clusters. Upon increasing χN , $\overline{\phi}_B(r=0)$ increases slowly for $\chi N<(\chi N)_{\rm odt}^{\rm scf}$, reaching approximately 0.4 at the next displayed value of $\chi N=34.8$. The value $\overline{\phi}_B(r=0)$ then increases much more rapidly from 0.4 to 0.8 over a much narrower range $\chi N=34.8$ to 39.2 that includes $(\chi N)_{\rm odt}^{\rm scf}=36.6$.

The average value $\phi_B(r)$ shown in Fig. 3a presumably contain contributions both from diffuse geometrical clusters and from proper micelles with nearly pure B-rich cores. To distinguish these subpopulations, we have computed the probability distribution for the value of ϕ_B defined within a small spherical region of radius r_c around the COM. We refer to this quantity as the core volume fraction, denoted by $\phi_B^{(c)}$. We use a value $r_c = 1.5\sigma$, indicated by the vertical line in Fig. 3a, giving $c\Delta V = 21.2$.

The probability distribution for $\phi_B^{(c)}$ is shown in Fig. 3b at several values of χN . At values of $\chi N = 0$ and 34.8 that are less than $(\chi N)_{\rm odt}^{\rm scf}$, we obtain a broad mono-

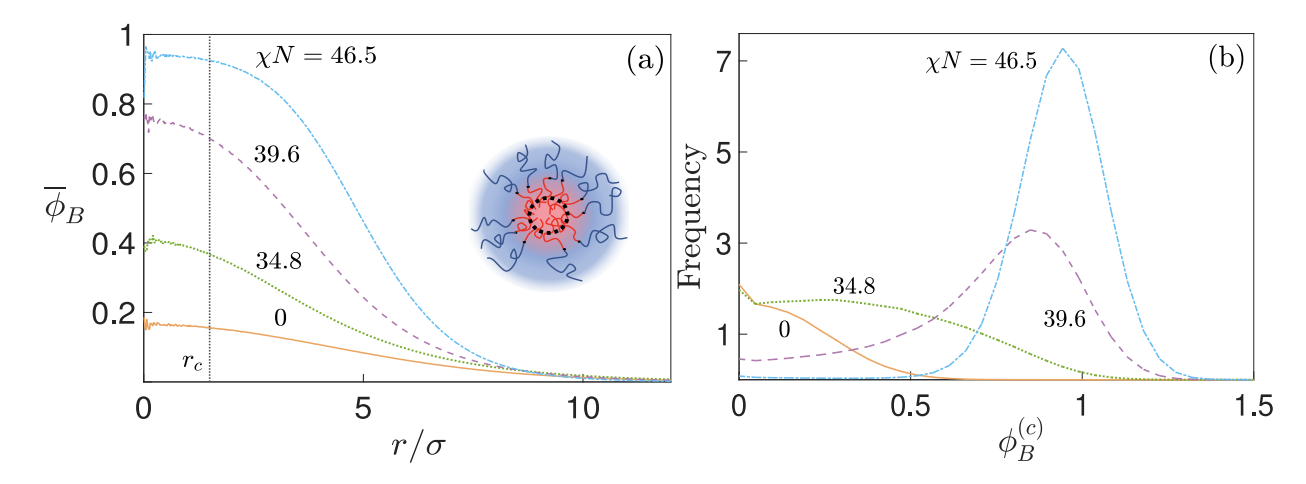


FIG. 3. (a) Local volume fraction $\overline{\phi}_B(r)$ of B (minority) block beads belonging to the cluster vs. distance r from the center of mass of these beads, at $\chi N=0$, 34.8, 39.6, and 46.5. (b) Probability distribution for the core volume fraction $\phi_B^{(c)}$ at the same χN values. The micelle schematic in plot (a) shows the inner core region of radius $r_c=1.5\sigma$ used to define $\phi_B^{(c)}$.

tonically decreasing distribution that is very small at $\phi_B^{(c)} \simeq 1$, characteristic of diffuse geometrical clusters. At values of $\chi N > (\chi N)_{\rm odt}^{\rm scf}$, however, we observe a local maximum at a most probable value of $\phi_B^{(c)}$ that rapidly approaches 1 with increasing χN , indicating the appearance of proper micelles with a nearly pure core. Note that our definition of $\phi_B = m_B/c\Delta V$ leads to some instantaneous values $\phi_B^{(c)} > 1$, when the total number of beads in the sampled volume is less than the average $c\Delta V$.

Figure 4 shows the evolution of the mean and most probable values of the core volume fraction $\phi_B^{(c)}$ with χN . The discontinuous jump in the most probable value of $\phi_B^{(c)}$ from zero to a large nonzero value signals the appearance of a distinct population of proper micelles with a very B-rich core. Note that this jump in the most probable value with increasing χN occurs very near the value $\chi N = (\chi N)_{\rm odt}^{\rm scf}$, indicated by a vertical line.

We focus in this article primarily on the onset of micellization, rather than micelle crystallization. We have, however, attempted to place bounds on the ODT by running simulations of systems with $\chi N = 41.9, 46.5$ and 50.9 from disordered and artificially ordered initial states while monitoring for spontaneous crystallization and spontaneous melting, respectively. These simulations were performed using periodic simulation unit cells designed accomodate $2 \times 2 \times 2$ or $3 \times 3 \times 3$ cubic unit cells of a BCC lattice (16 or 54 micelles), assuming a BCC unit cell length commensurate with the value of q^* measured in the disordered state at the same value of χN . In simulations designed for $3 \times 3 \times 3$ unit cells, we observed spontaneous melting for $\chi N = 41.9$ but never observed spontaneous crystallization. In simulations designed for $2 \times 2 \times 2$ unit cells, we observed spontaneous melting for $\chi N < 41.9$ and spontaneous crystallization for $\chi N = 46.5$ and 50.9. The evidence indicates an ODT

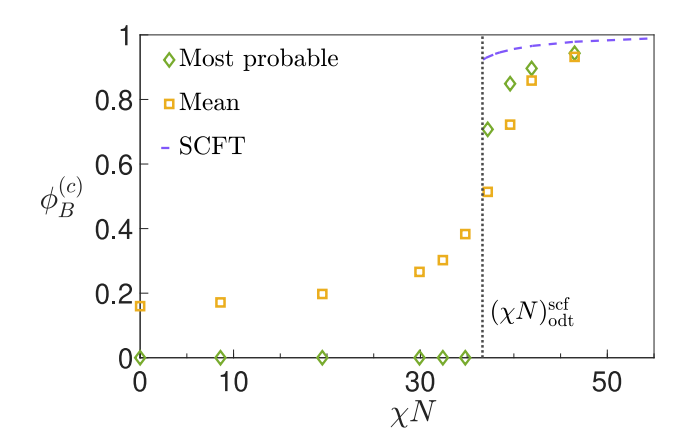


FIG. 4. Most probable (diamonds) and mean (square) values of the core volume fraction $\phi_B^{(c)}$ vs. χN . The vertical dotted line indicates $\chi N = (\chi N)_{\rm odt}^{\rm scf} = 36.6$. The dashed blue line shows SCFT predictions for $\phi_B(r=0)$ for $\chi N > (\chi N)_{\rm odt}^{\rm scf}$.

value $(\chi N)_{\rm odt} > 41.9$, though the exact value remains uncertain, and may be susceptible to finite size effects. Further details of this study are given in the Supplemental Material [44].

The results presented here provide a clear picture of the appearance of disordered micelles within a model melt of asymmetric diblock copolymers. The most direct evidence for the appearance of micelles comes from a cluster analysis in which micelles are identified as geometrical clusters that contain a nearly pure core of minority block beads. The results indicate that such micelles appear over a rather narrow range of values of χN centered very near the SCFT ODT value. This conclusion is consistent both with the predictions of Wang and coworkers [10], who assumed the validity of SCFT predictions for the free energy of an isolated micelle, and with the results of previous simulation studies that have

shown the somewhat surprising quantitative accuracy of SCFT predictions for properties of ordered phases and individual aggregates [16, 17, 43]. Our ability to make meaningful comparisons of simulations to SCFT predictions relied critically on relatively recent development of improved methods for calibrating χ in simulation models [16, 17]. To a very good approximation, it thus appears that the CMT in a melt of long, sphere-forming diblock copolymers corresponds to the SCFT ODT, and that the actual ODT occurs at a somewhat greater value of χN . We expect the onset of micellization at $\chi N \simeq (\chi N)_{\rm odt}^{\rm scf}$ to become more sudden with increasing \overline{N} , and for $(\chi N)_{\rm odt}$ to decrease with increasing \overline{N} , but further study would be required to test these hypotheses.

Our computational results have several important implications for experiments. Our data for S(q) provide new insights into the interpretation of SAXS and SANS experiments [2, 3, 7], which indicate that identification of a CMT by scattering alone may be difficult in systems with experimentally relevant values of \overline{N} . In the systems studied here, for which the value of $\overline{N} = 3820$ is greater than in many experiments, onset of micellization is signalled by the appearance of an initially small secondary shoulder in S(q) and by an inflection in a plot $S^{-1}(q^*)$ vs. χN , both of which arise from increased scattering associated with the appearance of micelles. Simulations of systems with lower \overline{N} , which we will report elsewhere, indicate that both features become less distinct with decreasing \overline{N} . Our comparison of results for S(q) to cluster analysis will aid interpretation of future experiments. Our results are also consistent with experimental evidence for the existence of micelles over a significant range of temperatures, despite remaining uncertainty regarding the location of the ODT for this simulation model. Our results establish that $(\chi N)_{\text{odt}}$ for this model exceeds $(\chi N)_{\text{odt}}^{\text{scf}}$ by at least 14%, and possibly much more, since we were only able to establish a lower bound on $(\chi N)_{\text{odt}}$. Theory, experience with more symmetric diblock copoolymers, and our own preliminary results for systems with lower \overline{N} (to be presented elsewhere) all suggest that the difference $(\chi N)_{\rm odt} - (\chi N)_{\rm odt}^{\rm scf}$ increases with decreasing \overline{N} . Further work is needed to determine the precise dependence of $(\chi N)_{\text{odt}}$ on N, and to study dynamical processes in the disordered phase near the ODT, which are directly relevant to the remarkable history dependence seen in recent studies of phase transformations in sphere-forming diblock copolymers [31–33]. The present contribution provides a cornerstone for more detailed study of the disordered micellar state by simulation.

This work was supported primarily by NSF grant DMR-1719692, using computational resources provided by the Minnesota Supercomputing Institute (MSI) at the University of Minnesota. Part of this work was carried out with equipment supported by funding from the National Science Foundation through the UMN MRSEC un-

der Award Number DMR-2011401.

- * email: dorfman@umn.edu
- † email: morse012@umn.edu
- D. Kinning and E. Thomas, Macromolecules 17, 1712 (1984).
- [2] M. Schwab and B. Stühn, Phys. Rev. Lett. 76, 924 (1996).
- [3] M. Schwab and B. Stühn, Colloid and Polymer Science 275, 341 (1997).
- [4] J. Adams, D. Quiram, W. Graessley, R. Register, and G. Marchand, Macromolecules 29, 2929 (1996).
- [5] J. K. Kim, H. H. Lee, S. Sakurai, S. Aid, J. Masomoto, S. Nomura, Y. Kitagawa, and Y. Suda, Macromolecules 32, 6707 (1999).
- [6] C. D. Han, N. Y. Vaidya, D. Kim, G. Shin, D. Yamaguchi, and T. Hashimoto, Macromolecules 33, 3767 (2000).
- [7] X. Wang, E. E. Dormidontova, and T. P. Lodge, Macromolecules 35, 9687 (2002).
- [8] J. N. Israelachvili, Intermolecular and surface forces, 3rd ed. (Academic Press, Amsterdam, 2011).
- [9] E. E. Dormidontova and T. P. Lodge, Macromolecules 34, 9143 (2001).
- [10] J. Wang, Z.-G. Wang, and Y. Yang, Macromolecules 38, 1979 (2005).
- [11] G. H. Fredrickson and E. Helfand, J. Chem. Phys. 87, 697 (1987).
- [12] K. T. Delaney and G. H. Fredrickson, J. Phys. Chem. B 120, 7615 (2016).
- [13] M. W. Bates, J. Lequieu, S. M. Barbon, R. M. Lewis III, K. T. Delaney, A. Anastasaki, C. J. Hawker, G. H. Fredrickson, and C. M. Bates, Proc. Natl. Acad. Sci. USA 116, 13194 (2019).
- [14] T. M. Beardsley, R. K. W. Spencer, and M. W. Matsen, Macromolecules 52, 8840 (2019).
- [15] M. W. Matsen, J. Chem. Phys. 152, 110901 (2020).
- [16] J. Glaser, P. Medapuram, T. M. Beardsley, M. W. Matsen, and D. C. Morse, Phys. Rev. Lett. 113, 068302 (2014).
- [17] P. Medapuram, J. Glaser, and D. C. Morse, Macromolecules 48, 819 (2015).
- [18] M. Yadav, F. S. Bates, and D. C. Morse, Phys. Rev. Lett. 121, 127802 (2018).
- [19] T. Vidil, N. Hampu, and M. A. Hillmyer, ACS Central Sci. 3, 1114 (2017).
- [20] N. Hampu and M. A. Hillmyer, ACS Appl. Polym. Mater. 1, 1148 (2019).
- [21] N. Hampu, M. W. Bates, T. Vidil, and M. A. Hillmyer, ACS Appl. Nano. Mater. 2, 4567 (2019).
- [22] N. Hampu and M. A. Hillmyer, ACS Macro Lett. 9, 382 (2020).
- [23] G. Ungar, Y. Liu, X. Zeng, V. Percec, and W.-D. Cho, Science 299, 1208 (2003).
- [24] X. Zeng, G. Ungar, Y. Liu, V. Percec, A. E. Dulcey, and J. K. Hobbs, Nature 428, 157 (2004).
- [25] S. Lee, M. J. Bluemle, and F. S. Bates, Science 330, 349 (2010).
- [26] M. Huang, C.-H. Hsu, J. Wang, S. Mei, X. Dong, Y. Li, M. Li, H. Liu, W. Zhang, T. Aida, W.-B. Zhang, K. Yue,

- and S. Z. Cheng, Science 348, 424 (2015).
- [27] K. Yue, M. Huang, R. L. Marson, J. He, J. Huang, Z. Zhou, J. Wang, C. Liu, X. Yan, K. Wu, Z. Guo, H. Liu, W. B. Zhang, P. Ni, C. Wesdemiotis, W. B. Zhang, S. C. Glotzer, and S. Z. Cheng, Proc. Natl. Acad. Sci. USA 113, 14195 (2016).
- [28] S. A. Kim, K. J. Jeong, A. Yethiraj, M. K. Mahanthappa, J. Jeong, A. Yethiraj, and M. K. Mahanthappa, Proc. Natl. Acad. Sci. USA 114, 4072 (2017).
- [29] C. M. Baez-Cotto and M. K. Mahanthappa, ACS Nano 12, 3226 (2018).
- [30] Z. Su, C.-h. Hsu, Z. Gong, X. Feng, J. Huang, R. Zhang, Y. Wang, J. Mao, C. Wesdemiotis, T. Li, S. Seifert, W. Zhang, T. Aida, M. Huang, and S. Z. D. Cheng, Nat. Chem. 11, 899 (2019).
- [31] K. Kim, M. W. Schulze, A. Arora, R. M. Lewis III, A. Hillmyer, K. D. Dorfman, and F. S. Bates, Science 356, 520 (2017).
- [32] K. Kim, A. Arora, R. M. Lewis, M. Liu, W. Li, A.-C. Shi, K. D. Dorfman, and F. S. Bates, Proc. Natl. Acad. Sci. USA 115, 847 (2018).
- [33] S. Jeon, T. Jun, S. Jo, H. Ahn, S. Lee, B. Lee, and D. Y. Ryu, Macromol. Rapid Commun. 40, 1900259 (2019).

- [34] L. Leibler, Macromolecules 13, 1602 (1980).
- [35] M. W. Matsen and M. Schick, Phys. Rev. Lett. 72, 2660 (1994).
- [36] G. H. Fredrickson, The equilibrium theory of inhomogeneous polymers (Clarendon Press, Oxford, 2006).
- [37] G. M. Grason, B. A. DiDonna, and R. D. Kamien, Phys. Rev. Lett. 91, 058304 (2003).
- [38] N. Xie, W. Li, F. Qiu, and A. C. Shi, ACS Macro Lett. 3, 906 (2014).
- [39] P. Grzywacz, J. Qin, and D. C. Morse, Phys. Rev. E 76, 061802 (2007).
- [40] D. C. Morse and J. K. Chung, J. Chem. Phys. 130, 224901 (2009).
- [41] J. Glaser, J. Qin, P. Medapuram, and D. C. Morse, Macromolecules 47, 851 (2014).
- [42] T. Ghasimakbari and D. C. Morse, Macromolecules **51**, 2335 (2018).
- [43] T. Ghasimakbari and D. C. Morse, Macromolecules 53, 7399 (2020).
- [44] See Supplemental Material at [URL will be inserted by publisher] for further details of MD simulations and analysis.

Identifying a Critical Micelle Temperature in Simulations of Disordered Asymmetric Diblock Copolymer Melts: Supplementary Material

Anshul Chawla, Frank S. Bates, Kevin D. Dorfman, and David C. Morse Department of Chemical Engineering and Materials Science, University of Minnesota, 421 Washington Ave. SE, Minneapolis, MN 55455, USA

SIMULATION DETAILS

Simulations presented in the main text are constant temperature, constant pressure (NPT) simulations of a model studied in previous work, which was referred to as model S2 in Refs. [1, 2]. Simulations are performed on a melt of diblock copolymers with N=64 beads per chain, with 8 B beads and 56 A beads.

Pairs of beads of types i and j that are separated by a distance r less than a cutoff length σ interact via a nonbonded pair potential

$$V_{\text{pair}}(r) = \frac{1}{2} \epsilon_{ij} \left(1 - \frac{r}{\sigma} \right)^2 \quad , \tag{S1}$$

with $V_{\text{pair}}(r) = 0$ for $r > \sigma$, where ϵ_{ij} is interaction energy parameter, with $\epsilon_{AA} = \epsilon_{BB}$. Neighboring beads within each chain interact via an additional harmonic bond potential

$$V_{\text{bond}}(r) = \frac{1}{2}\kappa r^2 \tag{S2}$$

with a spring constant κ .

All simulations were performed with fixed values of $\epsilon_{AA}/k_BT = 25$, $\kappa\sigma^2/k_BT = 1.135$, $P\sigma^3/k_BT = 4.111$ that were chosen for this model in previous work. Simulations were performed at multiple values of a parameter

$$\alpha = (\epsilon_{AB} - \epsilon_{AA})/k_B T \tag{S3}$$

in order to vary the effective χ parameter. Values of α used here are tabulated in Table S1.

This model and choice of constant parameters was shown to lead a statistical segment length b=1.727 and a monomer concentration $c=1.5\sigma^{-3}$ in the limit $\alpha\to 0$ and $N\to\infty$ of infinite homopolymers. The calibration of the effective χ parameter reported in Refs. [1] and [2] was found to give an effective χ parameter

$$\chi(\alpha) = \frac{0.0916\alpha - 0.00087\alpha^2}{1 + 0.0042\alpha} \quad . \tag{S4}$$

All values of χN reported here for simulations were computed using Eq. (S4), and are tabulated in Table S1.

All simulations were performed using the Hoomd-blue GPU accelerated MD engine [3, 4] in a periodic $L \times L \times L$ cubic unit cell with a fluctuating cell length L, using a symplectic, reversible NPT integrator. All simulations used a time step of 0.005 in natural simulation units in which k_BT , σ and bead mass are all equal to one.

α	χN	M	$NM N_{\rm step} \times 10^{-6}$		$\langle L \rangle / \sigma$
0	0	6803	435392	5392 30	
1.5	8.6	6803	435392 27		66.4
3.5	19.5	6803	435392	435392 27	
4.5	24.8	6803	435392	435392 27	
5.5	29.6	6803	435392	27	66.6
6	32.4	6803	435392	57	66.6
6.5	34.8	6803	435392	57	66.6
7	37.2	6803	435392	77	66.6
8	41.9	6803	435392	77	66.6
7	37.2	10149	649536	87	76.1
7.5	39.6	9194	588416	87	73.6
8	41.9	9081	581184	87	73.3
9	46.5	8879	568256	313	72.7
10	50.9	9384	600576	117	74.0

TABLE S1. Input parameters for simulation of the disordered phase. Here, M is the number of chains, N=64 is the number of beads per chain, N_{step} is the number of simulations steps in the simulation after initial equilibration, and $\langle L \rangle$ is the average length of one side of the cubic simulation cell. Simulations have been divided into three groups separated by horizontal lines, depending which of the three strategies described in the main text was used to choose M. The first group of simulations, for which M=6803, use an RPA box. The second group, for which $7 \leq \alpha \leq 8$, use an SCFT box. The third group, for which $\alpha=9$ or 10, use a commensurate box.

In simulations designed to probe properties of the disordered phase, the number of molecules used in each simulation, denoted by M, was chosen to create a system approximately large enough to accommodate a $3\times3\times3$ array of cubic unit cells of a hypothetical BCC crystal if the system were to crystallize. Three different strategies were used to estimate the required number of molecules in different parameter ranges:

(1) For all $\chi N < (\chi N)_{\rm odt}^{\rm scf}$ ($\alpha \leq 6.5$) and $\chi N = 37.2$ and 41.9 ($\alpha = 7$ and 8), simulations were performed using a target simulation unit cell length L that is designed to be commensurate with the RPA prediction for q^* in the disordered phase, such that the primary family of Bragg scattering peaks in the ordered phase would have a wavenumber equal to q^* . We refer to this in what follows as an RPA box.

- (2) For $\chi N=37.2$, 39.6 and 41.9 ($\alpha=7.0$, 7.5 and 8.0), simulations were performed using a target simulation cell length three times the SCFT prediction for the equilibrium length of the ordered BCC unit cell length. We refer to this as an SCFT box.
- (3) At $\chi N=46.5$ and 50.9 ($\alpha=9$ and 10) the target simulation cell length was chosen so as to be commensurate with the value of q^* measured in simulations. The estimates of q^* required to design these simulations were obtained in these cases by extrapolating values of q^* measured in earlier simulations performed at slightly lower values of χN . We refer to this as a commensurate box.

In each strategy, the calculated value for the target simulation unit cell length L is converted into a value for M by setting $M = cL^3/N$ with N = 64 and $c = 1.5\sigma^{-3}$ and rounding M to the nearest integer. Resulting values of M are given in Table S1.

STRUCTURE FACTOR

The structure factor of the melt is computed at values of wavevector \mathbf{q} that are commensurate with the instantaneous simulation unit cell length L, given by $\mathbf{q} = (2\pi/L)(h,k,l)$ with integer values of h, k, and l. The value of S(h,k,l) associated with a triplet of integers (h,k,l) is computed from the time average

$$S(h, k, l) = \left\langle \frac{1}{V} |\psi(h, k, l)|^2 \right\rangle \quad , \tag{S5}$$

in which $V = L^3$ and

$$\psi(h, k, l) \equiv \frac{1}{2} \sum_{i=1}^{NM} \epsilon_i e^{i\mathbf{q} \cdot \mathbf{r}_i} \quad , \tag{S6}$$

where i is a bead index, \mathbf{r}_i is the position of bead i, and $\epsilon_i = +1$ for B monomers and -1 for A monomers.

Each value of S(q) given in plots of S(q) vs. qR_{g0} is actually an average of values of S(h,k,l) for a family of wavevectors that are related by cubic point group symmetry operations, i.e., by permutations and/or inversions of the associated integer indices h, k and l. Each such family of symmetry-related wavevectors can be uniquely identified by a list of indices $\{h,k,l\}$ with $h \geq k \geq l \geq 0$. The value of q used to compute abscissa values for each symbol in such plots is an average wavenumber $q = \langle 2\pi/L \rangle \sqrt{h^2 + k^2 + l^2}$.

Values of the peak wavenumber q^* and peak intensity $S(q^*)$ have been obtained by fitting results for S(q) from each simulation to a fitting form

$$S(q) = KS_{RPA}(q) \quad , \tag{S7}$$

in which K is an adjustable fitting parameter, and $S_{RPA}(q)$ is the structure factor predicted by the randomphase approximation (RPA). The quantity $S_{RPA}(q)$ can be expressed as a function

$$S_{RPA}(q) = \frac{cN}{F(qR_{g0}, f) - 2\chi N}$$
 , (S8)

in which $F(qR_{g0}, f)$ is a known dimensionless function [5], and $R_{g0} = \sqrt{Nb^2/6}$ is the unperturbed radius of gyration. Values of q^* and $S(q^*)$ are obtained by using the fitting form shown in Eq. (S7) while treating K, χN and R_{g0} as fitting parameters for this purpose.

Note that the convention for the structure factor S(q) given in Eq. (S5) includes a normalization by the simulation unit cell volume V, rather than the more common convention of normalizing by the total number of beads in the system. This leads to an expression in which S(h, k, l) and S(q) have dimensions of inverse volume, and leads to a factor of monomer concentration c in Eq. (S8) that is absent in the expression given by Leibler [5].

Statistical errors for the value of S(q) associated with each family of symmetry related wavevectors have been computed using the hierarchical block averaging analysis of Flyvbjerg and Petersen [6]. A sequence of instantaneous values of S(q) for each family of equivalent wavevectors is obtained by sampling every 1000 time steps and averaging results for $|\psi(h,k,l)|^2$ over wavevectors that are related by cubic symmetry operations. The resulting sequence is then divided into blocks of different lengths that differ by factors of 2, with 2^n sequential measurements per block at blocking level n, such that the trajectory is divided into only a few blocks for the maximum value of n. A block average is computed for each such block. An estimate of the error on the time average is computed for each level of blocking by treating block averages as if they were statistically independent, though this is not true for short block lengths. A final error estimate is obtained by an algorithm that automatically identifies a range of block lengths that give consistent error estimates, corresponding to a "plateau" in a plot or tabulation of the error estimate vs. n. Such a plateau will exist if and only if the simulation length is significantly longer than the autocorrelation time of the quantity being measured, giving ergodic sampling of that quantity. The lengths of our simulations were chosen so as to guarantee that this method yields consistent error estimates for S(q) for wavenumbers $q \sim q^*$ for which autocorrelation times are longest and statistical errors are largest.

Table S2 presents numerical results for $S(q^*)$ and q^* at different values α , as obtained by fitting S(q) to the RPA functional form. Estimates of the error on the peak intensity $S(q^*)$ given here represent the root mean squared deviation of the actual values of S(q) from the fit for values q within 10 % of the estimated value of q^* .

Fig S1 show results for the ratio $S(q^*)/S_{RPA}(q^*)$ vs. χN . The value of $S_{RPA}(q^*)$ used to compute this ratio is calculated using values for χN that were obtained from Eq. (S4), as reported in Table S1. This representation

α	χN	$S(q^*)/cN$	q^*R_{g0}
0	0	0.010 ± 0.00003	2.312
1.5	8.6	0.013 ± 0.000006	2.298
3.5	19.5	0.019 ± 0.00014	2.297
4.5	24.8	0.024 ± 0.00012	2.281
5.5	29.6	0.035 ± 0.00025	2.271
6	32.4	0.045 ± 0.00004	2.236
6.5	34.8	0.067 ± 0.00031	2.202
7	37.2	0.125 ± 0.00116	2.158
7.5	39.6	0.284 ± 0.00305	2.110
8	41.9	0.552 ± 0.00136	2.099
9	46.5	1.415 ± 0.03323	2.069

TABLE S2. Nondimensionalized peak intensity $S(q^*)/cN$ and peak wavenumber qR_{g0} at different χN .

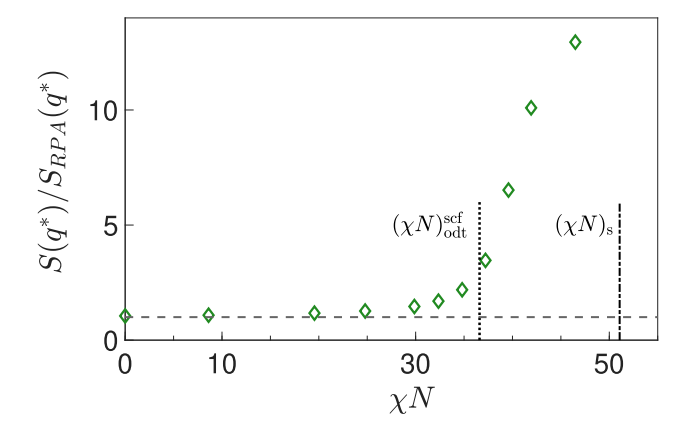


FIG. S1. Ratio $S(q^*)/S_{RPA}(q^*)$ of the actual peak intensity $S(q^*)$ to the RPA prediction $S_{RPA}(q^*)$ plotted vs. χN . Symbols show simulation results. The horizontal long-dashed line indicates the RPA prediction $S(q^*)/S_{RPA}(q^*)=1$. The vertical dotted line labelled $(\chi N)_{\rm odt}^{\rm scf}$ indicates the SCFT ODT. The vertical dot-dashed line labelled $(\chi N)_{\rm s}$ indicates the RPA spinodal.

makes it clear that an increase in peak intensity $S(q^*)$ above that predicted by the RPA begins at approximately $\chi N=30$ and increases most rapidy with increasing χN at values slightly above $(\chi N)_{odt}^{scf}$. The same results are shown as a plot of $cNS^{-1}(q^*)/2$ vs. χN in Fig. 1 of the main manuscript.

Fig. S2 shows the dependence of q^* on χN . The RPA prediction of $q^*R_{g0}=2.271$ is shown by a horizontal line. Note the significant difference between this RPA prediction and the values predicted by SCFT for the primary Bragg scattering peak q^* in either ordered phase near the ODT, which predicts $q^*R_{g0}=1.872$ in the FCC phase at $\chi N=(\chi N)_{\rm odt}^{\rm scf}$. The magnitude of this difference motivated us to test the consistency of results obtained using an RPA or SCFT box in this range of values of χN .

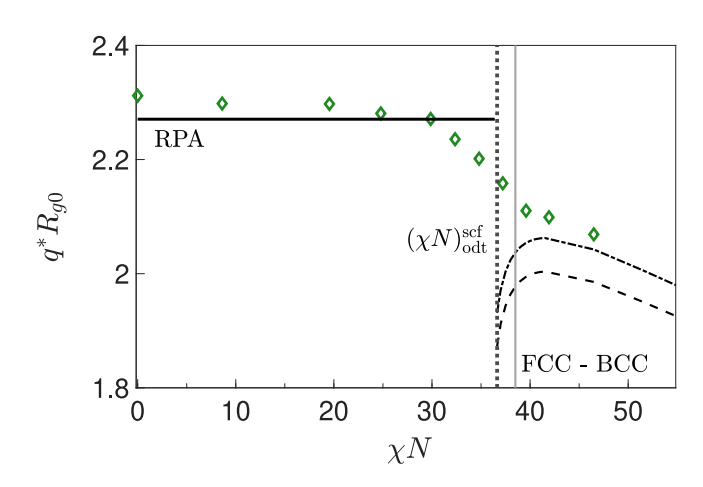


FIG. S2. Normalized peak scattering wavenumber q^*R_{g0} vs. χN , where $R_{g0} = b\sqrt{N/6}$. Symbols show simulation results. Solid horizontal line is the RPA prediction. The vertical dotted line represents the value $(\chi N)_{odt}^{scf} = 36.6$ at which SCFT predicts a transition from a disordered to an FCC phase. The solid gray vertical line marked FCC-BCC marks the value of $\chi N = 38.5$ at which SCFT predicts an FCC-BCC orderorder transition. The dot-dash line and dashed line shown for $\chi N > (\chi N)_{\rm odt}^{\rm scf}$ are SCFT predictions of q^*R_{g0} for the primary Bragg scattering peak within the BCC phase and FCC phases, respectively, with the larger value of q^*R_{g0} corresponding to the BCC phase.

At $\chi N=37.2$ and 41.9 ($\alpha=7$ and 8), simulations were performed using two different values of M obtained by different strategies in order to test the sensitivity of our results to finite size effects. Each plot in Fig. S3 shows a comparison of values of the structure factor S(q) obtained using an RPA box to those obtained using an SCFT box. At both values of χN , values of S(q) obtained with these different system sizes appear to be consistent to within known statistical errors, confirming that these results are rather insensitive to finite size effects within the range of sizes used here.

Fig. S4 shows a corresponding comparison of results for the cluster histogram x_n vs. n obtained from simulations performed at $\chi N=37.2$ and 41.9 using the RPA and SCFT boxes. For $\chi N=37.2$, results obtained with these different system sizes are indistinguishable. For $\chi N=41.9$, the difference becomes visible, but remains too small to affect any of our conclusions. We have not computed rigorous statistical errors for values of x_n , and thus cannot say whether the results for x_n obtained with different box sizes at $\chi N=41.9$ are consistent within statistical errors.

BREAKDOWN OF ERGODICITY

Results of measurements of of S(q) from a simulation performed at $\chi N = 50.9$ indicate that this system is not ergodic over the time scale accessible in our simulations.

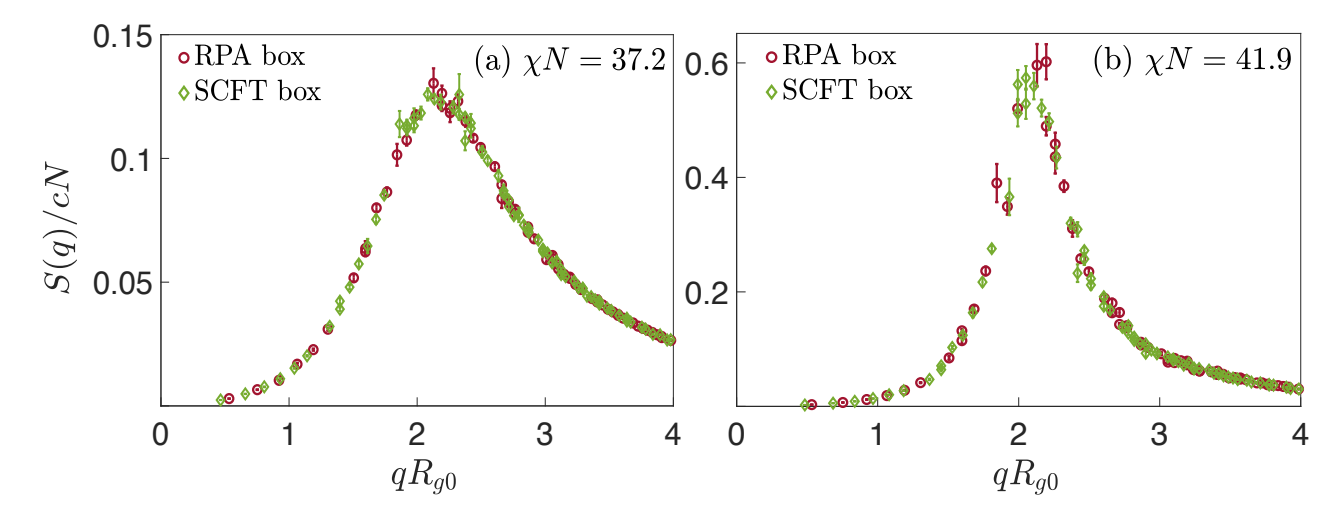


FIG. S3. Comparison of results for S(q) vs. qR_{g0} obtained in simulations with RPA and SCFT boxes at (a) $\chi N = 37.2$ and (b) $\chi N = 41.9$.

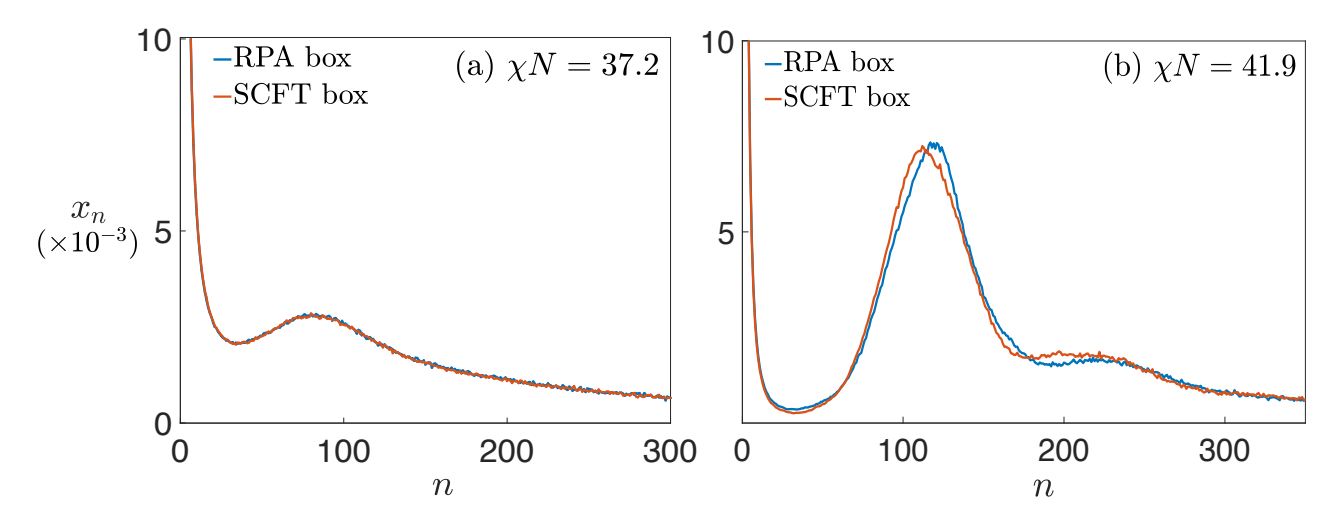


FIG. S4. Comparisons of results for the mole fraction x_n of chains in clusters of aggregation number n from simulations with RPA and SCFT boxes, for (a) $\chi N = 37.2$ and (b) $\chi N = 41.9$.

We thus show physical properties of the disordered phase only for $\chi N \leq 46.5$ ($\alpha \leq 9$) in Table S2, Figs. S1 and S2 and all figures of the main manuscript.

Fig. S5 shows a comparison of results for S(q) vs. qR_{q0} obtained in simulations performed at $\chi N = 46.5$ and 50.9 using commensurate boxes designed to accomodate a $3 \times 3 \times 3$ array of BCC unit cells. Each symbol in these plots represents an average value of S(q) for a family of symmetry related wavevectors. The two dotted vertical lines in each of these plots identify values of qR_{a0} for which two different families of symmetryrelated wavevectors happen to yield the same value for the wavenumber $q = \langle (2\pi/L) \rangle \sqrt{h^2 + k^2 + l^2}$. One of these is the value of qR_{a0} arising from the {410} and {322} families, which both yield $h^2 + k^2 + l^2 = 17$. The other is the value of qR_{g0} arising from the {330} and {411} families, for which $h^2 + k^2 + l^2 = 18$. Values of M for these simulations were chosen so as to yield a wavenumber for the {330} family equal to an estimated value of q^* . For $\chi N = 46.5$ this procedure succeeded, since the maximum values of S(q) are obtained for the $\{330\}$ and $\{411\}$ families. For $\chi N = 50.9$, the maximum value of S(q) is instead obtained for the {331} family.

In the case of ergodic sampling of a fluid in a sufficiently large periodic simulation cell, we expect S(q) to become a smooth function of q alone. Specifically, we expect to obtain consistent results for S(q) from different families of wavevectors that yield exactly equal values of q. This expectation is met for results obtained at $\chi N = 46.5$, but not at $\chi N = 50.9$. In results for $\chi N = 50.9$ shown in Fig. S5b, there are large, statistically significant differences between pairs of values of S(q) that lie along one of the vertical dotted lines shown in this figure. For the {410} and {322} families, which both yield $qR_{g0} = 1.97$, the larger value of S(q) arises from the {410} family. For the {330} and {411} families, which both yield $qR_{q0} = 2.03$, the larger value arises from the {411} family. In contrast, for the case $\chi N = 46.5$ shown in Fig. S5, the values of S(q) from these pairs of wavevector families appear to be consistent to within known statistical errors, which are indicated here by error bars that show a range within one standard deviation

Discrepancies in values of S(q) obtained from different families of symmetry-related wavevectors with the same wavenumber could in principle be either a result non-ergodic sampling or, conceivably, of ergodic sampling of a system with a large finite-size effect. An equilibrium finite size effect in a fluid confined to a periodic cubic simulation cell would give rise to results that preserve cubic symmetry, and thus give equivalent scattering intensities for wavevectors in the same family. To distinguish these possibilities, we have examined contributions to S(q) that arise from individual wavevectors, rather than from families of wavevectors that are related by cubic symmetry. Fig. S6 shows results for S(q) at $\chi N = 50.9$ plotted

without any averaging over families of wavevectors, with contributions from individual wavevectors plotted as separate symbols. Because exactly equal values of $S(\mathbf{q})$ are obtained from wavevectors \mathbf{q} and $-\mathbf{q}$ that are related by inversion, each symbol in this plot shows the scattering from one member of such a pair of wavevectors. Inspection of the results show that time averages for different wavevectors within each family differ by much more than statistical errors computed for individual wavevectors. This is clear in this figure from the fact, that along each of the three dotted vertical lines, there is a single symbol that is greater than all others at the same value of qR_{a0} by differences much greater than the error bars. The existence of signficant differences in scattering from wavevectors that are related by symmetry indicates that this simulation was not long enough to adequately sample the disordered state. The simplest reason for this would be if the system were stuck in a single disordered spatial arrangement of micelles for the entire length of the simulation.

MELTING AND CRYSTALLIZATION

A separate set of simulations were performed to place bounds on the value $(\chi N)_{\rm odt}$ of χN at the ODT, by looking for spontaneous melting and crystallization. Melting and/or crystallization simulations were performed at $\chi N=41.9,\ 46.5,\ {\rm and}\ 50.9.$ Both melting and crystallization simulations were performed in a commensurate box that is designed to accomodate either a $2\times 2\times 2$ or a $3\times 3\times 3$ array of BCC unit cells. Specifically, the number M of molecules for an $n\times n\times n$ array of BCC unit cells is chosen so as to give a target simulation unit cell size size $L=(MN/c)^{1/3},\ {\rm computed}\ {\rm using}\ c=1.5\sigma^{-3},\ {\rm for}\ {\rm which}\ {\rm the}\ {\rm wavenumber}\ q=2\sqrt{2\pi}n/L\ {\rm of}\ {\rm the}\ \{nn0\}\ {\rm family}\ {\rm of}\ {\rm wavevectors}\ {\rm that}\ {\rm yields}\ {\rm the}\ {\rm first}\ {\rm BCC}\ {\rm Bragg}\ {\rm scattering}\ {\rm peak}\ {\rm is}\ {\rm equal}\ {\rm to}\ {\rm an}\ {\rm estimate}\ {\rm of}\ {\rm the}\ {\rm peak}\ {\rm wavenumber}\ q^*$ measured in the disordered phase.

Crystallization simulations are performed in such a commensurate unit cell with a disordered initial state. Melting simulations are performed using an artificially ordered BCC initial state. This artificial ordered state is created by running a preliminary simulation in the presence of a periodic external field that favors accumulation of B monomers at the desired locations of micelle cores, and using the final state of this simulation as the initial state of a "melting" simulation performed with no external ordering field.

Table S3 tabulates values of α , χN and system sizes for melting and crystallization simulations. For each choice of system size $(2 \times 2 \times 2 \text{ or } 3 \times 3 \times 3)$, both melting and crystallization simulations were performed at $\chi N = 46.5$ and 50.9, while only a melting simulation was performed at $\chi N = 41.9$. At $\chi N = 46.5$ and 50.9, the simulations with a commensurate $3 \times 3 \times 3$ unit cell that we used

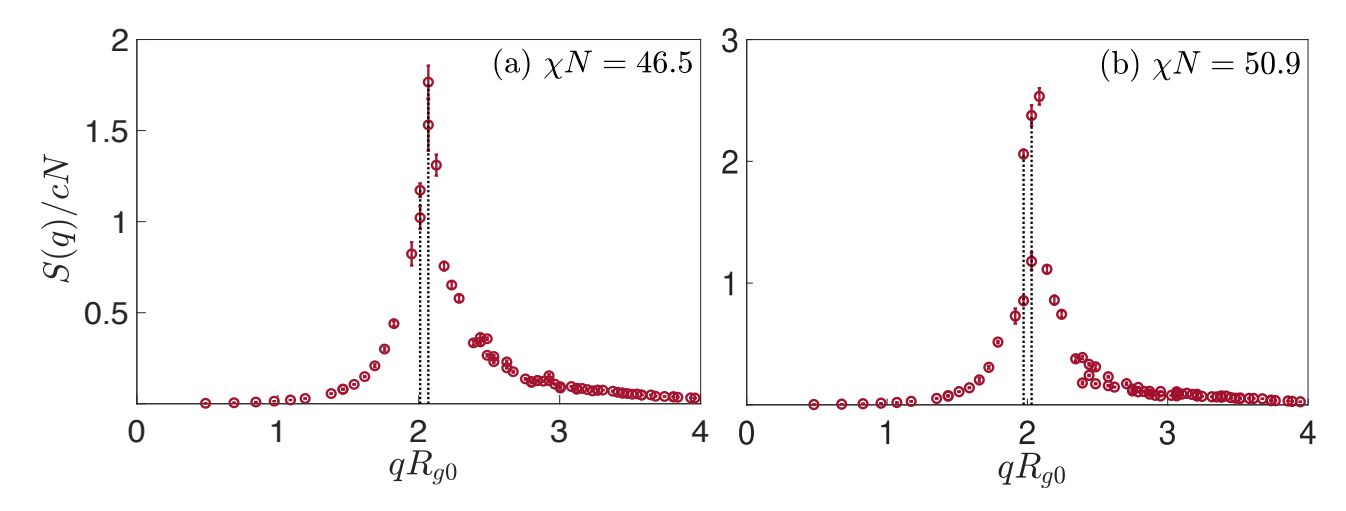


FIG. S5. (a) Structure factor at $\chi N = 46.5$. (a) Structure factor at $\chi N = 50.9$. Dotted vertical lines indicate values of qR_{g0} that are each associated with two different families of symmetry-related wavevectors, as discussed in the text.

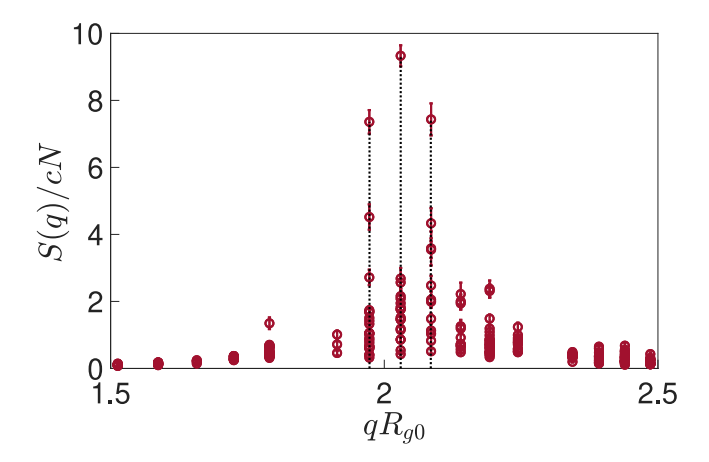


FIG. S6. Structure factor in the liquid phase at $\chi N = 50.9$, with contributions of individual wavevectors plotted separately. The three vertical dotted lines show values of qR_{g0} for wavevectors with integer indices (h, k, l) for which $h^2 + k^2 + l^2 = 17$, 18 and 19.

to monitor for crystallization (which did not occur) were also used to study properties of the disordered phase.

The difference between a disordered phase and a perfect BCC crystal is apparent upon visualization of the final state, or upon inspection of plot of S(q) vs. qR_{g0} obtained from a time average over a period near the end of a melting or crystallization simulation. Fig. S7 shows a plot of S(q) vs. qR_{g0} obtained from the time average of a "melting" a simulation performed using an artificially ordered $3\times 3\times 3$ array of BCC unit cells at $\chi N=46.5$, for which the crystal persisted over the length of the simulation. The existence of a BCC crystal is clearly evident from the existence of several Bragg peaks with intensities much greater than those of peaks that do not belong to the reciprocal lattice of the BCC crystal.

In simulations of $3 \times 3 \times 3$ unit cells, spontaneous melt-

ing was observed at $\chi N=41.9$, but spontaneous crystallization was not observed at either $\chi N=46.5$ or 50.9. In simulations of $2\times 2\times 2$ unit cell, spontaneous melting was observed at $\chi N=41.9$ and spontaneous crystallization was observed at both $\chi N=46.5$ and 50.9. We can conclude that the equilibrium value of $(\chi N)_{\rm odt}$ for a $2\times 2\times 2$ unit cell is somewhere in the range [41.9,46.5], and that $(\chi N)_{\rm odt}$ for a $3\times 3\times 3$ unit cell is greater than 41.9.

We do not know how much the ODT is altered by the use of such small unit cells. We expect finite size effects to stabilize the crystal phase when the system size is commensurate with q^* , as is true here, and when the correlation length for composition fluctuations becomes comparable to or greater than the simulation cell length. When these conditions are satisfied, we expect the true equilibrium value of $(\chi N)_{\rm odt}$ in such a finite commensurate system to be lower than that of a hypothetical infinite system. The peak in S(q) shown in Fig. S5a, for $\chi N=46.5$ and a $3\times 3\times 3$ system, is quite narrow.

α	χN	BCC cells	M	$N_{\rm step} \times 10^{-6}$	type
8	41.9	$2 \times 2 \times 2$	2661	100	melting
9	46.5	$2 \times 2 \times 2$	2631	200	melting
9	46.5	$2 \times 2 \times 2$	2631	200	crystallization
10	50.9	$2 \times 2 \times 2$	2781	200	crystallization
8	41.9	$3 \times 3 \times 3$	8982	60	melting
9	46.5	$3 \times 3 \times 3$	8879	60	melting
9	46.5	$3 \times 3 \times 3$	8879	316	crystallization
10	50.9	$3 \times 3 \times 3$	9384	120	crystallization

TABLE S3. Parameters of melting and crystallization simulations performed to estimate the ODT.

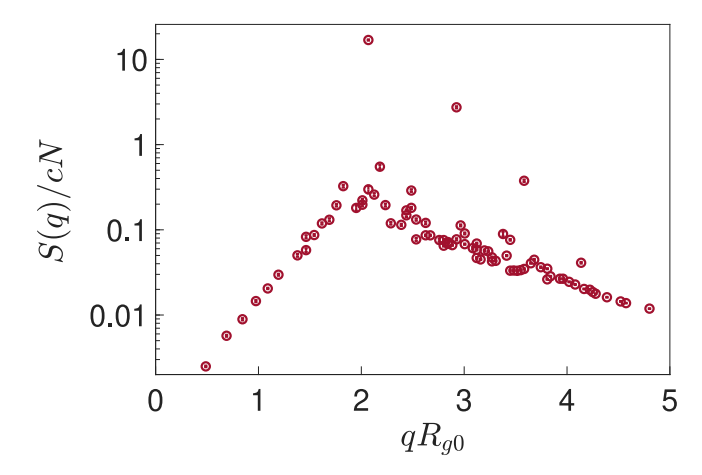


FIG. S7. Structure factor in the BCC phase at $\chi N=46.5$, showing the existence of a sequence of Bragg peaks with intensities approximately one order of magnitude greater than the intensities obtained for wavevectors that do not satisfy the Bragg scattering condition.

In this case, the peak width has become comparable to the distance between allowed values of q, which indicates that the correlation length is becoming comparable to the system size at this value of χN even in the $3\times 3\times 3$ system. Finite size effects are presumably more severe at the same value of χN in the metastable liquid phase of a smaller $2\times 2\times 2$ system, though spontaneous crystal-

lization prevents S(q) from being measured for this case. Further study with careful attention to consequences of both finite size effects and slow dynamics will be needed to reliably identify ODTs in simulations of sphere forming systems. This article instead focuses primarily on characterizing the onset of micellization within the disordered phase.

- J. Glaser, P. Medapuram, T. M. Beardsley, M. W. Matsen, and D. C. Morse, "Universality of block copolymer melts," Phys. Rev. Lett. 113, 068302 (2014).
- [2] Pavani Medapuram, Jens Glaser, and David C. Morse, "Universal phenomenology of symmetric diblock copolymers near the order-disorder transition," Macromolecules 48, 819–839 (2015).
- [3] Joshua A. Anderson, Chris D. Lorenz, and A Travesset, "General purpose molecular dynamics simulations fully implemented on graphics processing units," J. Comput. Phys. 227, 5342–5359 (2008).
- [4] Jens Glaser, Trung Dac Nguyen, Joshua A. Anderson, Pak Lui, Filippo Spiga, Jaime A. Millan, David C. Morse, and Sharon C. Glotzer, "Strong scaling of general-purpose molecular dynamics simulations on gpus," Comput. Phys. Commun. 192, 97–107 (2015).
- [5] Ludwik Leibler, "Theory of microphase separation in block copolymers," Macromolecules 13, 1602–1617 (1980).
- [6] H. Flyvbjerg and H.G. Petersen, "Error estimates on averages of correlated data," J. Chem. Phys. 91, 461–466 (1989).